Medium-range structure of vitreous SiO_2 obtained through first-principles investigation of vibrational spectra

Luigi Giacomazzi,[1,2,3] P. Umari,[1,2,4] and Alfredo Pasquarello[1,2]
[1]*Institute of Theoretical Physics, Ecole Polytechnique Fédérale de Lausanne (EPFL), CH-1015 Lausanne, Switzerland*
[2]*Institut Romand de Recherche Numérique en Physique des Matériaux (IRRMA), CH-1015 Lausanne, Switzerland*
[3]*CNR-INFM/Democritos National Simulation Center and the Abdus Salam International Centre for Theoretical Physics (ICTP), Strada Costiera 11, I-34014 Trieste, Italy*
[4]*Theory @ Elettra Group, CNR-INFM/Democritos, Area Science Park Basovizza, I-34012 Trieste, Italy*
(Received 29 October 2008; revised manuscript received 16 December 2008; published 9 February 2009)

Using a density-functional framework, we investigate the vibrational spectra of vitreous SiO_2 to determine to what extent these spectra provide information about the medium-range structure of the oxide network. We carry out a comparative study involving three model structures, which all feature a nondefective network of corner-sharing tetrahedra but differ through their Si-O-Si bond-angle distributions and ring statistics. We first address the results of typical diffraction probes. Fair agreement with experiment is achieved for the total neutron and total x-ray structure factors of all models, indicating limited sensitivity of these structure factors to the medium-range structure. The same consideration also applies to the Si-O and O-O partial structure factors. At variance, the Si-Si partial structure factor is found to be highly sensitive to the Si-O-Si bond-angle distribution. We then address typical vibrational spectra, such as the inelastic neutron spectrum, the infrared spectra, and the Raman spectra. For the inelastic neutron spectrum and the infrared spectra, the comparison with experiment is fair for all models, indicating poor sensitivity to the structural arrangement of tetrahedra. The only noticeable exception is the feature at ~ 800 cm^{-1} which shifts to higher frequencies with decreasing Si-O-Si angles. At variance, the Raman spectra are shown to be very informative about the medium-range organization of the network through their sensitivity to the concentrations of three-membered and four-membered rings. Our study indicates that the considered experimental data are globally consistent with a medium-range structure characterized by an average Si-O-Si bond angle of 148° and with small-ring concentrations as derived from the intensities of the experimental Raman defect lines. To describe the infrared and Raman couplings, our work also introduces parametric models which reproduce well the spectra calculated from first principles.

DOI: 10.1103/PhysRevB.79.064202 PACS number(s): 63.50.Lm, 78.30.−j, 61.43.Fs, 71.15.Mb

I. INTRODUCTION

Vitreous silica (v-SiO_2) is a technologically important material, being a key component in both optical fibers[1] and Si-based microelectronic devices.[2] From the fundamental point of view, v-SiO_2 has attracted attention as the archetypical model of a disordered network.[3] These motivations have contributed to making v-SiO_2 one of best characterized materials through the application of a large variety of experimental probes.

The short-range structure of v-SiO_2 is fully characterized by the occurrence of a well-defined tetrahedral structural unit,[4] consisting of a central silicon atom with oxygen atoms at its vertices. The tetrahedra are attached to each other through their corners, giving rise to an extended network. The medium-range structure of v-SiO_2 is less trivial. The disorder is essentially carried by the broad distribution of the intertetrahedral bond-angle parameter. The analysis of diffraction[5–7] and nuclear-magnetic-resonance data[8,9] situate the average Si-O-Si bond angle close to 150°. The medium-range structure is further characterized by the ring statistics.[10] While such a characterization has long remained a purely theoretical concept, it has recently been possible to derive concentrations of three-membered and four-membered rings from the experimental Raman spectrum.[11,12]

To acquire deeper insight into the structure of disordered oxides beyond nearest neighbors, it is necessary to consider experimental probes in addition to the typical diffraction probes. A potentially informative set of data consists of the vibrational spectra, such as the inelastic neutron spectrum, the infrared spectra, the Raman spectra, and the hyper-Raman spectra. However, the interpretation of vibrational spectra in terms of structural correlations is not trivial and requires accurate theoretical modeling. Such modeling approaches need to overcome several difficulties which include the generation of viable model structures, the accurate determination of vibrational properties, and the access to the coupling factors. For this scope, suitable modeling tools have been developed within a density-functional framework, one of the most noteworthy being the method consisting of applying finite electric fields through a Berry-phase formulation.[13] In the last decade, these modeling approaches were at the origin of several successful applications to vitreous materials, including SiO_2,[11,12,14–17] GeO_2,[18,19] B_2O_3,[20] and $GeSe_2$.[21] The ultimate aim of such modeling approaches is to determine a model structure which optimally describes the full set of experimental data under consideration. It is imagined that this scope can be achieved by the establishment of a virtuous cycle including model generation, simulation of measurable quantities, and comparison with experiment.

In this work, we carry out a comprehensive investigation of the structural and vibrational properties of v-SiO_2 within a density-functional framework. Particular attention is devoted

to the comparison with experimental results. As far as the more traditional structural probes are concerned, we address the total neutron structure factor, the total x-ray structure factor, and the partial structure factors. For the vibrational properties, our study comprises the inelastic neutron spectrum, the dielectric constants, the real and imaginary parts of the dielectric function, the energy-loss spectrum, the LO-TO splittings, and the Raman spectra. The present work includes a comparative study involving three model structures presenting similar short-range order but different intertetrahedral bond-angle distributions and ring statistics. More specifically, our study aims at identifying specific features in the vibrational spectra which are informative about the medium-range structure. For the purpose of the present work, we considered a 144-atom model structure (model I) incorporating structural features inferred from previous investigations with the aim of improving the comparison with the experiment for the full set of vibrational spectra under consideration. Finally, we conclude our study by deriving simple parametric models which account for the infrared and Raman couplings. The motivation for developing such models is twofold. First, the description of the coupling factors in terms of a limited set of parameters necessarily requires the identification of the dominating coupling terms, providing insight into the most significant underlying physical mechanisms. Second, the availability of such models gives access to the vibrational spectra without requiring the calculation of the coupling factors, thereby facilitating further refinements of structural models. We note that parts of the results pertaining to model I were used in a previous publication for a comparison between vitreous SiO_2 and vitreous GeO_2.[22]

This paper is organized as follows. Section II gives a brief description of the applied methodological scheme. The models of v-SiO_2 used in this work are introduced in Sec. III. This section describes their origin, their short-range and medium-range structural properties, and their electronic structure. In Sec. IV, we obtain the vibrational frequencies and eigenmodes of our models, which are at the basis of all the subsequent calculations in this work. In particular, we compare in this section the vibrational densities of states (v-DOSs) of the three models. Section V is devoted to the calculation of structure factors as obtained by neutron and x-ray diffractions. We focus on the total neutron structure factor, the total x-ray structure, and the individual partial structure factors. For all these quantities, we carry out comparisons with their experimental counterparts. This section also addresses the pair-correlation functions. In Sec. VI, we start our study of the vibrational spectra by considering the inelastic neutron spectra of our models. The calculated spectra are compared to experimental ones. Infrared spectra are obtained and discussed in Sec. VII. Our study includes the static and high-frequency dielectric constants, the Born charge tensors, the real and imaginary parts of the dielectric function, the energy-loss spectrum, and the LO-TO splittings. This section also introduces a simple parametric model for the description of the infrared coupling. Section VIII addresses the Raman spectra. We obtain Raman spectra for all our models and discuss to what extent these spectra reflect medium-range structural properties of the oxide network. This section concludes with the derivation of optimal bond-polarizability parameters to describe the Raman coupling in v-SiO_2. The conclusions of our work are drawn in Sec. IX.

II. METHODS

The electronic and structural relaxations were carried out within a first-principles scheme[23,24] based on density-functional theory. The exchange and correlation energy was accounted for through the local-density approximation (LDA) to density-functional theory. Plane-wave basis sets with energy cutoffs of 25 and 200 Ry were used to expand the electron wave functions and the electron density, respectively. Core valence interactions were accounted for by a norm-conserving pseudopotential for Si (Ref. 25) and an ultrasoft one for O.[26] The wave functions were expanded at the sole Γ point of the Brillouin zone, as justified by the large size and the large band gap of our systems. We used computer codes as provided in the QUANTUM-ESPRESSO package.[27]

For obtaining the vibrational frequencies and eigenmodes, we calculated the analytical part of the dynamical matrix by taking finite differences of the atomic forces upon sequential displacement of all atoms.[14,28] In these calculations, we used atomic displacements of ± 0.1 bohr, which correspond to a regime in which the atomic forces show a linear dependence on the displacement. Alternatively, the dynamical matrix could be obtained in a fully equivalent way through a perturbational approach.[29,30]

The calculation of the infrared and Raman spectra requires the evaluation of the first and second derivatives of the atomic forces with respect to the electric field.[16] In the present work, these calculations were carried out through a scheme which allows one to consider finite electric fields in periodic density-functional calculations.[13] The relevant derivatives could then be obtained numerically by finite differences. The values of the applied electric fields are constrained to the interval of fields for which the calculation converges,[13] but should be chosen sufficiently large to achieve good numerical accuracy. For the infrared spectra, the Born charge tensors result from the first derivatives of the atomic forces with respect to the electric field. For the Raman spectra, the second derivatives are needed and are calculated as outlined in Appendix A.

In the limit of large simulation cells, it has been demonstrated that this approach is fully equivalent to the treatment of electric fields within perturbational schemes.[13] A discussion concerning the convergence with increasing simulation cell can be found in Ref. 31. To provide an estimate of residual errors, we compared in Sec. VIII C optimal bond-polarizability parameters as derived through the application of finite electric fields to those obtained within a perturbational approach.

III. MODELS OF VITREOUS SILICA

A. Origin of models

The use of multiple models constitutes a way to achieve a good level of statistical representation of the structural features of v-SiO_2.[32] Thus, for discussing the structural and vi-

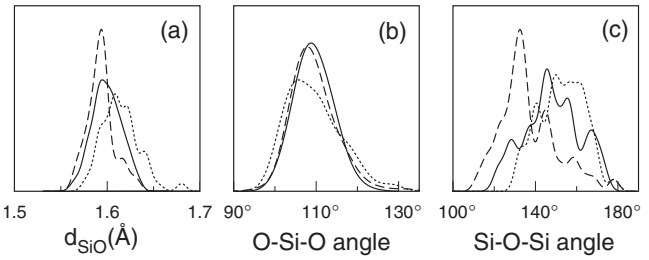

FIG. 1. Distributions of (a) Si-O bond lengths, (b) O-Si-O bond angles, and (c) Si-O-Si bond angles for models I (solid curve), II (dotted curve), and III (dashed curve) of v-SiO_2. Gaussian broadenings of 0.005 Å and 2.5° were used.

brational properties of v-SiO_2, we considered a set of three models. All models considered in this work correspond to a network of corner-sharing tetrahedra without any coordination defect. The simulation cells are cubic and the structures were subject to periodic boundary conditions. The cell parameters were kept fixed in order to reproduce the experimental density of 2.2 g/cm^3.

Model I was generated for the purpose of this work through the combined use of classical and first-principles molecular dynamics.[16,33] In case of vitreous silica and vitreous germania, the use of such a combined scheme allows one to obtain models with structural and vibrational properties of comparable quality to those generated within fully first-principles schemes.[18,34] As a starting point for the generation of model I, we selected a model structure of v-SiO_2 among those previously generated in Ref. 33 by classical molecular dynamics.[35,36] Good agreement with the experimental Si-O-Si bond-angle distribution and a low content of three-membered rings (cf. Sec. III C) were used as selection criteria. The selected model structure then underwent structural optimization through damped first-principles molecular dynamics.[23,24] Model I consists of 144 atoms. For comparison, the set of models considered in this work also includes two smaller structures of only 72 atoms, generated in previous studies. Model II was generated in the same way as model I,[11] whereas model III was obtained within a fully first-principles scheme.[37]

B. Short-range structure

In the following, we primarily focus on model I and use the other two models for comparison. In Fig. 1(a), we show the bond-length distributions of our models. All three models show very similar average bond lengths (~1.6 Å) in good agreement with experimental estimates.[6] The bond-length distribution of model I most closely resembles a Gaussian distribution, as a consequence of the larger size of this model and therefore of the larger statistical sampling of bonds. The spread of bond lengths is smallest for model III, suggesting that a fully *ab initio* generation procedure[37] improves the quality of the structural relaxation. In Fig. 1(b), we show the O-Si-O bond-angle distribution for our models. In all the models, the average O-Si-O bond angle is very close to the experimental value corresponding to the ideal tetrahedral geometry (109.47°).[6] For model II the width of this distribution is slightly larger than for the other two models, witnessing some residual strain in the tetrahedra. In Fig. 1(c), we show the Si-O-Si bond-angle distributions of models I–III. The average values of the Si-O-Si bond-angle distributions are reported in Table I. The Si-O-Si bond-angle distribution is a key quantity for the description of a network of corner-sharing tetrahedra. Indeed, it relates to the way the tetrahedra are arranged, thereby defining the medium-range order of the network. Model II shows the largest average angle (153°) and is characterized by a distribution of rather large angles, ranging between 130° and 180°. On the other hand, model III shows a predominance of small angles, with an average angle of only 137°. Model I shows an intermediate distribution ranging between 120° and 180° with an average angle of 148°. The average angles of both model I and model II are consistent with experimental measurements which indicate a value close to 150°.[5–9]

TABLE I. Structural properties of models I–III of v-SiO_2: number of atoms (N), average bond length (d_{SiO}), average O-Si-O angle, and average Si-O-Si angle. The respective standard deviations are given in parentheses. Experimental estimates for the angles and the bond lengths are taken from Ref. 6.

	N	d_{SiO} (Å)	∠O-Si-O	∠Si-O-Si
Model I	144	1.600 (0.015)	109.4° (4.3°)	148.2° (13.4°)
Model II	72	1.614 (0.020)	109.5° (6.4°)	152.6° (10.9°)
Model III	72	1.594 (0.014)	109.5° (5.3°)	136.9° (14.2°)
Expt.		1.605	109.47°	148.3°

C. Medium-range structure: Ring statistics

Vitreous SiO_2 can be thought as a random network in which the basic topological units are the SiO_4 tetrahedra.[3] To characterize the connectivity of the network, a medium-range-order property, it is convenient to have recourse to the ring statistics.[10,38] We here adopted the shortest path analysis proposed in Ref. 10, which allows direct comparison with previous ring-statistics studies of SiO_2.[12,36,39,40] The ring statistics of our three models of v-SiO_2 are shown in Fig. 2. For all the models, five-membered and six-membered rings are the most frequent. The fact that the network of vitreous silica contains a large number of six-membered rings can be understood by considering the phase diagram of silica.[36] When the system is cooled from the liquid phase at zero pressure, the crystalline phase that is obtained is β-cristobalite,[41] which has only rings of size 6. Therefore, it can be expected

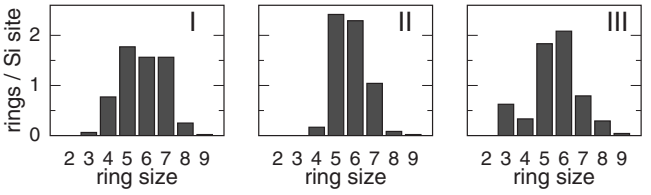

FIG. 2. Ring statistics of models I–III of v-SiO_2. The size specifies the number of Si-O segments.

TABLE II. Concentrations of O atoms belonging to three-membered (O_{3R}) and four-membered (O_{4R}) rings in our models of v-SiO_2 and estimates derived from the experimental Raman spectrum (Ref. 11).

	Model I	Model II	Model III	Ref. 11
O_{3R}	3%	0%	31%	0.22%
O_{4R}	42%	8.3%	17%	0.36%

that the local structure of the amorphous network resembles that of β-cristobalite with six-membered rings among the most frequent ones. In all our models, rings of size 8 or larger are rare. Comparing the models, we register significant differences for the concentration of three-membered and four-membered rings. Model I shows a single three-membered ring and ten four-membered rings. The sum of bond angles inside the three-membered ring amounts to 698°, slightly less than the ideal value of 720°. This indicates that the ring is quasiplanar.[12] In model II, three-membered rings are absent and only a single four-membered ring occurs. Model III shows five three-membered rings and two four-membered rings.[12]

In Table II, we give the concentration of O atoms belonging to three-membered and four-membered rings in our models of v-SiO_2. The values are compared with estimates derived from the experimental Raman spectrum.[11] In general, all models show significant deviations with respect to the experimental estimates. These deviations reflect, on the one hand, the difficulty of generating models with the targeted ring concentrations and, on the other hand, the inadequate size of the considered models. A model containing ~1000 atoms would be necessary to approach the theoretical estimate of O in three-membered rings, but this would be computationally prohibitive for first-principles calculations. Having these limitations in mind, we considered structural models with substantially different ring statistics in order to understand the effects of this property on the vibrational spectra. More specifically, model III shows concentrations of three-membered and four-membered rings exceeding the experimental estimates by 1–2 orders of magnitude. In particular, the occurrence of a large number of three-membered rings is expected to affect the medium-range properties in a severe way because of the small angles and the planarity of such structural units. Model II shows the lowest concentrations of small rings and thus the best agreement with the estimates derived from the experimental Raman spectrum. However, three-membered rings are absent in this model. Model I was selected with the intent of achieving concentrations of small rings close to those of model II, but with the occurrence of a single three-membered ring. Its concentration of three-membered rings is then determined by the size of the model (144 atoms). This choice further resulted in a concentration of four-membered rings in excess by 2 orders of magnitude. However, four-membered rings cause less stringent structural constraints than three-membered rings and are therefore expected to affect the vibrational properties in a milder way.

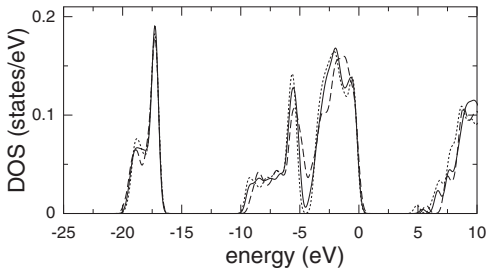

FIG. 3. Electronic DOSs of our models of v-SiO_2: model I (solid curve), model II (dotted curve), and model III (dashed curve). The energy scales are aligned through the O 2s states. The energy scale is referred to the top of the valence band of model I. The DOSs of models II and III have been rescaled to match the normalization of the DOS of model I. A Gaussian broadening of 0.25 eV was used.

D. Electronic structure

The electronic densities of states (DOSs) of the models under consideration are given in Fig. 3. The origin of the bands in terms of atomic orbitals is similar to the case of α-quartz SiO_2 (Ref. 42): the lowest band arises from O 2s states, the low-energy side of the central band results from the bonds between Si sp^3 and O 2p orbitals. The high-energy side of this central band consists of O 2p nonbonding orbitals, which define the top of the valence band. The low-energy part of the conduction band carries a predominant Si weight and results from antibonding combinations between Si sp^3 and O 2p orbitals.[42] For the purpose of comparison, the energy scales in Fig. 3 were aligned through the deep O 2s states, which are assumed to be least affected by the structural disorder. The electronic densities of states of the three models only show minor variations. In particular, we calculated band gaps of 5.4, 5.1, and 5.6 eV for models I, II, and III, respectively. The calculated band gaps severely underestimate the experimental value [~9 eV (Ref. 43)], as usual in density-functional schemes. The band-gap variations mainly results from different locations of the conduction-band minimum and should be attributed to the structural disorder. A similar behavior has also been observed for GeO_2.[44] The present electronic density of states is consistent with previous density-functional calculations for α-quartz and v-SiO_2.[37,42]

IV. VIBRATIONAL FREQUENCIES AND EIGENMODES

In this section, we address the vibrational properties of vitreous silica. The analytical part of the dynamical matrix is expressed using a similar notation as in Ref. 30:

$$D_{IiJj} = \frac{1}{\sqrt{M_I M_J}} \frac{\partial^2 E_{\text{tot}}}{\partial R_{Ii}\, \partial R_{Jj}} = -\frac{1}{\sqrt{M_I M_J}} \frac{\partial F_{Jj}}{\partial R_{Ii}}, \qquad (1)$$

where E_{tot} is the total energy of the system and M_I is the mass of the Ith atom. Uppercase and lowercase indices indicate the atoms and the three Cartesian directions, respectively. We obtained the dynamical matrix in Eq. (1) through a finite-difference scheme.[14,28]

The full dynamical matrix also includes a nonanalytical matrix, $\mathcal{D}^{\mathbf{q}}_{IiJj}$, accounting for vibrational excitations longitudinal to the normalized direction $\mathbf{q}$ along which the vibrational momentum is exchanged:[45]

$$D^{\mathbf{q}}_{IiJj} = D_{IiJj} + \mathcal{D}^{\mathbf{q}}_{IiJj}, \tag{2}$$

with

$$\mathcal{D}^{\mathbf{q}}_{IiJj} = \frac{1}{\sqrt{M_I M_J}} \frac{4\pi}{\epsilon_\infty V} \left(\sum_k Z^*_{I,ki} \cdot q_k \right) \left(\sum_h Z^*_{J,hj} \cdot q_h \right), \tag{3}$$

where V indicates the volume of the periodic simulation cell. In Eq. (3), the high-frequency dielectric tensor of our system is assumed to be isotropic.[19,20,46,47] The tensors $Z^*_{I,ik}$ entering in Eq. (3) are the Born effective charge tensors. These are defined as the polarization P^{el}_i along the direction i induced by a unitary displacement of the Ith atom in direction k (Ref. 48):

$$Z^*_{I,ik} = V \frac{\partial P^{\mathrm{el}}_i}{\partial R_{Ik}} = -\frac{\partial^2 E_{\mathrm{tot}}}{\partial \mathcal{E}_i \partial R_{Ik}} = \frac{\partial F_{Ik}}{\partial \mathcal{E}_i}. \tag{4}$$

The last equality gives an alternative definition of the Born effective charge tensors in terms of a derivative of the atomic force component F_{Ik} with respect to the electric field component $\mathcal{E}_i$. The derivative with respect to the electric field should be evaluated at vanishing electric field. In this work, we obtained the tensors $Z^*_{I,ik}$ by calculating these derivatives numerically by finite differences. An extended analysis of the Born charges is given in Sec. VII.

For a given choice of $\mathbf{q}$, the frequencies ω_n and the corresponding normalized eigenmodes $\boldsymbol{\xi}^n_I$ are obtained by diagonalizing the dynamical matrix. The associated atomic displacements are given by

$$\mathbf{u}^n_I = \frac{1}{\sqrt{M_I}} \boldsymbol{\xi}^n_I. \tag{5}$$

The index n labels the vibrational modes and runs from 1 to $3N$, where N is the total number of atoms in the model.

The v-DOS underlies all the vibrational spectra. The v-DOS $Z(\omega)$ is expressed in terms of the vibrational frequencies ω_n as

$$Z(\omega) = \frac{1}{3N} \sum_n \delta(\omega - \omega_n). \tag{6}$$

In Fig. 4(a), the vibrational density of states of model I is compared to those of models II and III.[14,16,28] The principal features are reproduced similarly in the three models, with the main peaks located approximately at the same energies. However, the position of the peak at ~100 meV differs noticeably among the models. This peak results from bending vibrations[28] and its position appears to be sensitive to the Si-O-Si bond-angle distribution, occurring at higher energy as the average Si-O-Si angle in the model decreases (cf. Table I).[51,52] For a detailed analysis of the vibrational density of states in terms of the underlying vibrations, we refer to Refs. 14 and 28.

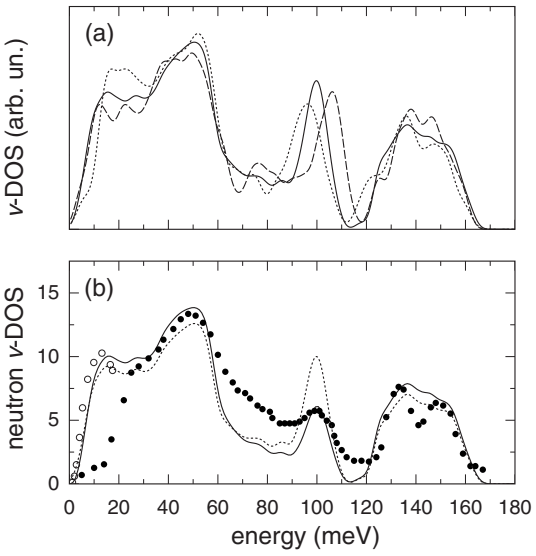

FIG. 4. (a) Calculated vibrational density of states of model I (solid curve) of v-SiO_2 compared to those of model II (dotted curve) and model III (dashed curve), taken from Refs. 14 and 16. (b) Calculated effective neutron density of states for model I (solid curve), compared to the experimental result from Ref. 49 (closed symbols) and to the actual vibrational density of states (dotted curve). Experimental data from Ref. 50 are also shown (open symbols). In the calculation, we used a temperature of 33 K and the Q range between 6 and 13 Å^{-1}, as in the experiment of Ref. 49. A Gaussian broadening of 2.5 meV was used in the calculation.

V. NEUTRON AND X-RAY STRUCTURE FACTORS

A. Pair-correlation functions

It is preferable to carry out the comparison between theory and experiment through the structure factors, as these quantities correspond to the direct measurements and do not undergo further manipulation. However, since real-space correlations carry a more intuitive character, we first illustrate the structural properties through the partial pair-correlation functions $g_{\alpha\beta}(r)$. In a binary system, the function $g_{\alpha\beta}(r)$ gives the ratio between the density of atoms of species β at a distance r from an atom of species α and the average density ρ_β of atoms of species β (Ref. 53):

$$g_{\alpha\beta}(r) = \frac{1}{N_\alpha \rho_\beta} \sum_{I\in\alpha, J\in\beta} \delta(r - |\mathbf{R}_J - \mathbf{R}_I|), \tag{7}$$

where N_α corresponds to the number of atoms of species α.

We accounted for finite-temperature effects in the pair-correlation functions by broadening the interatomic separations of the equilibrium structure through the use of Gaussian functions, their widths being determined by the vibrational eigenmodes and frequencies obtained in the harmonic approximation.[19,54] Specifically, we replaced the δ functions in Eq. (7) with Gaussian functions with a variance σ^2_{IJ} given by[54]

$$\sigma^2_{IJ} = \langle [\mathbf{d} \cdot (\mathbf{u}_I - \mathbf{u}_J)]^2 \rangle, \tag{8}$$

where $\mathbf{u}_I$ is the displacement of the Ith atom with respect to the equilibrium position $\mathbf{R}_I$, and $\mathbf{d}$ is a unit vector along the

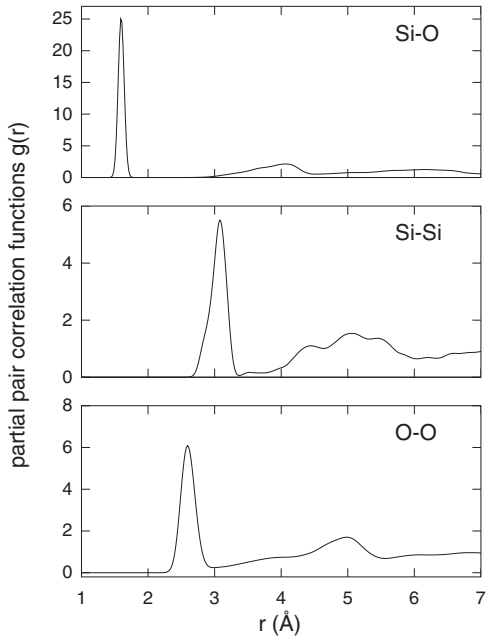

FIG. 5. Pair-correlation functions $g_{SiO}(r)$, $g_{SiSi}(r)$, and $g_{OO}(r)$ of model I of v-SiO_2, calculated in the harmonic approximation at room temperature.

direction of $\mathbf{R}_J - \mathbf{R}_I$. The brackets $\langle \cdots \rangle$ indicate a thermal average obtained as follows:[54]

$$\langle u_{Ii} u_{Jj} \rangle = \sum_n \frac{\hbar}{\omega_n} \frac{\xi^n_{Ii}}{\sqrt{M_I}} \frac{\xi^n_{Jj}}{\sqrt{M_J}} \left[n_B(\hbar\omega_n) + \frac{1}{2} \right], \tag{9}$$

where the indices i and j label the Cartesian directions, M_I corresponds to the mass of the Ith atom, and the temperature dependence enters through the boson occupation number

$$n_B(E) = \frac{1}{e^{E/k_B T} - 1}, \tag{10}$$

where k_B is the Boltzmann factor. This approach has been shown to be well suited for describing oxide glasses at room temperature.[54] It does not require extended molecular-dynamics runs and captures the zero-point motion effects.[54]

In Fig. 5, we give the pair-correlation functions of model I, $g_{SiO}(r)$, $g_{SiSi}(r)$, and $g_{OO}(r)$, evaluated at room temperature. The first peak of $g_{SiO}(r)$ is located at 1.59 Å and agrees closely with the Si-O bond length (Table I). From a spherical integration of the first peak in $g_{SiO}(r)$, we derive an average coordination number of 4, consistent with the absence of any coordination defect in our model. Similarly, spherical integration of the first peaks in $g_{SiSi}(r)$ and $g_{OO}(r)$ up to their respective minima yield values of 4.0 and 6.3, respectively. These average coordination numbers clearly indicate the occurrence of a network of corner-sharing tetrahedra, in which each Si atom is surrounded by the four Si atoms of the nearest-neighbor tetrahedra. The first peaks of $g_{SiSi}(r)$ and $g_{OO}(r)$ correspond to Si-Si and O-O distances of 3.08 and 2.59 Å, respectively.

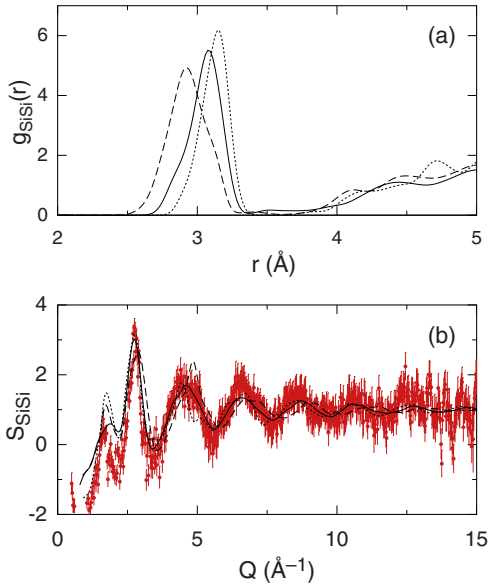

FIG. 6. (Color online) Comparison between (a) the Si-Si pair-correlation functions $[g_{SiSi}(r)]$ and (b) the Si-Si partial structure factors $[S_{SiSi}(Q)]$ of model I (solid curve), model II (dotted curve), and model III (dashed curve). Calculated results are obtained in the harmonic approximation at room temperature. We used a Gaussian broadening of 0.15 Å^{-1} in (b). The partial structure factors are compared with the experimental data of Ref. 7 (disks with error bars).

The most significant differences between the three models considered in this work appear in the Si-Si pair-correlation functions. Figure 6(a) shows that the location of the first peak of this pair-correlation function varies according to the Si-O-Si bond-angle distribution [Fig. 1(c)]. In particular, this peak is situated at 3.08, 3.15, and 2.92 Å for models I, II, and III, respectively. The peak position for model I (3.08 Å) is in particularly good agreement with a recent diffraction measurement which situates this peak at 3.08 ± 0.01 Å.[7] This agreement lends support to the value of 148.2° found in model I for the average Si-O-Si angle (Table I).

B. Neutron and x-ray structure factors

We express the total structure factor as a function of the exchanged momentum Q (Ref. 53),

$$S(Q) = \sum_{\alpha,\beta} (c_\alpha c_\beta)^{1/2} \frac{f_\alpha(Q) f_\beta(Q)}{\langle f^2(Q) \rangle} S_{\alpha\beta}(Q), \tag{11}$$

$$\langle f^2(Q) \rangle = \sum_\alpha c_\alpha f^2_\alpha(Q), \tag{12}$$

where $c_\alpha = N_\alpha / N$, f_α are atomic scattering factors, and $S_{\alpha\beta}(Q)$ are the partial structure factors in the Ashcroft-Langreth formulation:

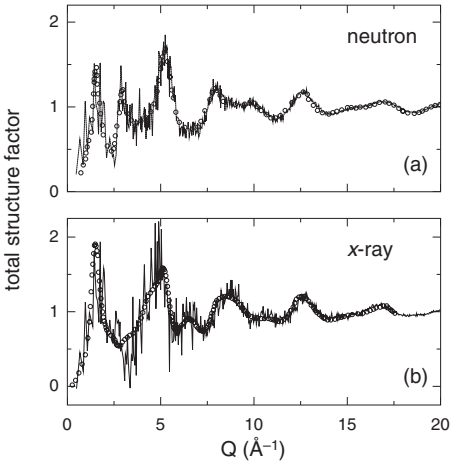

FIG. 7. (a) Calculated total neutron structure factor (solid curve) for model I of v-SiO_2 at room temperature, compared with its experimental counterpart (circles) (Ref. 58). (b) Calculated x-ray structure factor at room temperature (solid curve) for model I of v-SiO_2, compared with its experimental counterpart (circles) (Ref. 59).

$$S_{\alpha\beta}(Q) = \frac{1}{\sqrt{N_\alpha N_\beta}} \left\{ \left\langle \sum_{J\in\alpha, K\in\beta} e^{-i\mathbf{Q}\cdot(\mathbf{R}_J - \mathbf{R}_K)} \right\rangle - \delta_{\mathbf{Q},0} \right\}, \tag{13}$$

where the brackets $\langle \cdots \rangle$ indicate a thermal average. For isotropic materials, the structure factors only depend on the modulus of $\mathbf{Q}$, and are obtained by a spherical average.[55] Only $\mathbf{Q}$ vectors compatible with the periodicity of the simulation cell are retained. Therefore, the result corresponds to the infinitely repeated model.[56]

Adopting the harmonic approximation, the thermal average can be calculated by means of Eq. (9). The partial structure factors then simplify to

$$S_{\alpha\beta}(Q) = \frac{1}{\sqrt{N_\alpha N_\beta}} \left\{ \sum_{J\in\alpha, K\in\beta} e^{-W_{JK}(\mathbf{Q})} e^{i\mathbf{Q}\cdot(\mathbf{R}_J - \mathbf{R}_K)} - \delta_{\mathbf{Q},0} \right\}, \tag{14}$$

where the exponents in the Debye-Waller factors are given by

$$W_{JK}(\mathbf{Q}) = \frac{1}{2} \langle \{ \mathbf{Q} \cdot (\mathbf{u}_J - \mathbf{u}_K) \}^2 \rangle. \tag{15}$$

In neutron diffraction, the interactions between the incoming neutrons and the nuclei are described by the neutron-scattering lengths b_α: $f_\alpha(Q) = b_\alpha$. In our calculations, we took the neutron-scattering lengths $b_{Si} = 4.149$ fm and $b_O = 5.805$ fm.[57] We show in Fig. 7(a) the comparison between the neutron structure factors of model I and the experimental data taken from Ref. 58. Overall good agreement is registered with the experiment. The other two models show comparisons with experiment of similar quality.[16,37]

The x-ray structure factor is also given by Eq. (11),[53] where the $f_\alpha(Q)$ now stand for the atomic x-ray scattering factors.[60] Figure 7(b) shows the comparison between the x-ray structure factors of model I and the experimental data taken from Ref. 59. The agreement with experimental data is of similar quality to that registered for the neutron structure factor [Fig. 7(a)]. In the range of $Q \leq 5$ Å^{-1}, the x-ray structure factor differs markedly with respect to the neutron structure factor. In particular, in the x-ray structure factor the first sharp diffraction peak shows an increased intensity, and no feature is registered corresponding to the second peak in the neutron structure factor (~ 2.7 Å^{-1}). These differences result from the different atomic scattering factors in neutron and x-ray diffractions.

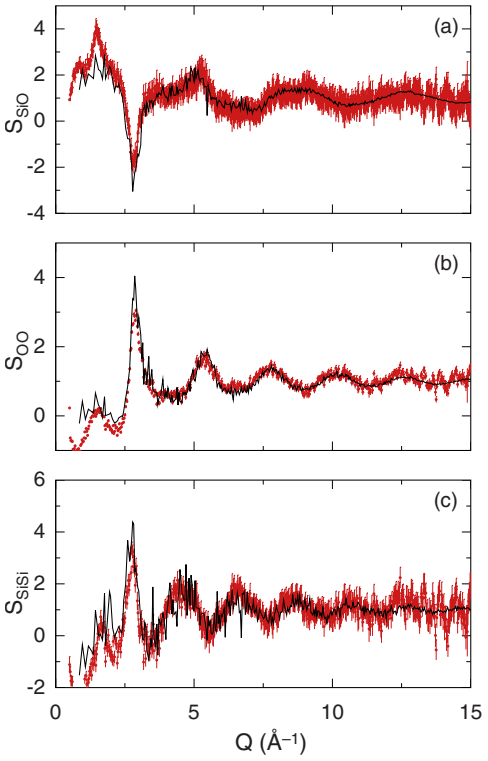

FIG. 8. (Color online) Faber-Ziman partial structure factors calculated for model I of v-SiO_2 at room temperature (solid curve), compared to experimental results from Ref. 7 (disks with error bars): (a) $S_{SiO}(Q)$, (b) $S_{OO}(Q)$, and (c) $S_{SiSi}(Q)$.

C. Partial structure factors

Very recently, the partial structure factors of vitreous silica have been measured.[7] We here carry out a detailed comparison between theory and experiment for these structure factors. The Faber-Ziman formulation of the partial structure factors is related to the common Ashcroft-Langreth form, $S_{\alpha\beta}(Q)$, through the following relations:[53]

$$S^{FZ}_{\alpha\alpha}(Q) = [S_{\alpha\alpha}(Q) - c_\beta]/c_\alpha, \tag{16}$$

$$S^{FZ}_{\alpha\beta}(Q) = S_{\alpha\beta}(Q)/(c_\alpha c_\beta)^{1/2} + 1, \tag{17}$$

where α and β indicate Si and O species, respectively. In Fig. 8, we show the Faber-Ziman partial structure factors calculated for model I at room temperature, compared to the experimental data of Ref. 7. We register very good overall

agreement, particularly above 3 Å^{-1}. The positions of the features occurring at ~2.7 Å^{-1} are generally also well described, but the theoretical features are slightly more pronounced than their experimental counterparts for each of the three partial structure factors. In the region of the first sharp diffraction peak, we observe the largest differences between theory and experiment. However, it should be mentioned that in this region the **Q** vectors available for the theoretical structure factors are more sparse because of the finite size of the model, which results in significant fluctuations between nearby values of Q.

To address the differences between the three model structures studied in this work, we focus on the Si-Si partial structure factor, which is the most informative about the Si-O-Si bond-angle distribution. In Fig. 6(b), the comparison involves the three models and experiment.[7] As for the Si-Si pair-correlation function [cf. Fig. 6(a)], the three models show noticeable differences. The best agreement between theory and experiment is achieved for model I. The description offered by model II is only marginally worse with the most significant differences confined in the region below 5 Å^{-1}. The disagreement with experiment is most apparent for model III, which shows a Si-Si structure factor with out-of-phase oscillations persisting up to high values of Q. The good agreement achieved for model I brings further support to its Si-O-Si bond-angle distribution.

In recent years, the partial structure factors of disordered network-forming systems have often been discussed[7,61,62] in the formulation proposed by Bhatia and Thornton.[63] The partial structure factors in this formulation are obtained from $S_{\alpha\beta}(Q)$ by the following linear transformation:[53]

$$S_{\mathrm{NN}}(Q) = c_\alpha S_{\alpha\alpha}(Q) + c_\beta S_{\beta\beta}(Q) + 2\sqrt{c_\alpha c_\beta} S_{\alpha\beta}(Q), \quad (18)$$

$$S_{\mathrm{CC}}(Q) = c_\alpha c_\beta [c_\beta S_{\alpha\alpha}(Q) + c_\alpha S_{\beta\beta}(Q) - 2\sqrt{c_\alpha c_\beta} S_{\alpha\beta}(Q)], \quad (19)$$

$$S_{\mathrm{NC}}(Q) = c_\alpha c_\beta \left[S_{\alpha\alpha}(Q) - S_{\beta\beta}(Q) + \frac{c_\beta - c_\alpha}{\sqrt{c_\alpha c_\beta}} S_{\alpha\beta}(Q) \right]. \quad (20)$$

In Fig. 9, we show the Bhatia-Thornton partial structure factors calculated for model I, compared with the experimental data from Ref. 7. Overall, we record similar agreement as for the Faber-Ziman partial structure in Fig. 8, with small differences between theory and experiment confined to the region below 3 Å^{-1}. We note that the $S_{\mathrm{NN}}(Q)$ is very similar to the neutron total structure factor. This can be understood by comparing Eqs. (11) and (18) and by taking into account the fact that O and Si have similar scattering lengths. In the limit $Q \to \infty$, the number-number structure factor $S_{\mathrm{NN}}(Q)$ tends to unity [Eq. (18)]. In the concentration-concentration structure factor $S_{\mathrm{CC}}(Q)$, the dominant peak is located at ~2.7 Å^{-1}. We do not register any clear trace of the first sharp diffraction peak, in agreement with the experiment[7] and previous calculations.[37] This behavior of vitreous silica has recently been assigned to the absence of coordination defects.[62] For large values of Q, the $S_{\mathrm{CC}}(Q)$ and $S_{\mathrm{NC}}(Q)$ tend to $c_\alpha c_\beta$ = 2/9 and 0, respectively [Eqs. (19) and (20)].

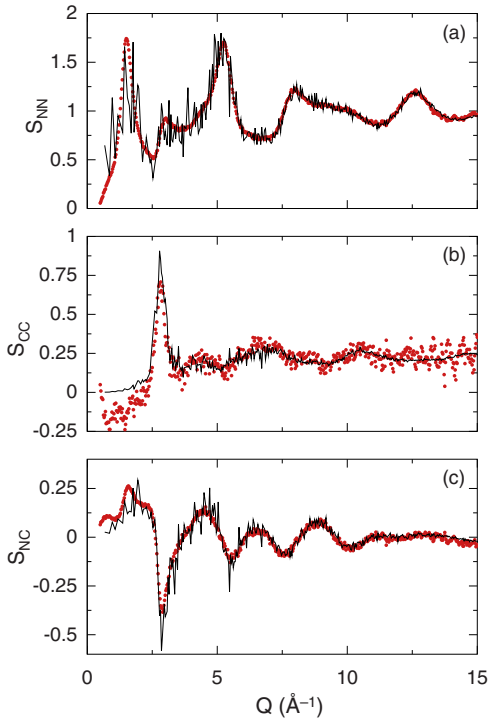

FIG. 9. (Color online) Bhatia-Thornton partial structure factors calculated for model I of v-SiO_2 at room temperature (solid curve), compared to experimental results from Ref. 7 (disks): (a) $S_{\mathrm{NN}}(Q)$, (b) $S_{\mathrm{CC}}(Q)$, and (c) $S_{\mathrm{NC}}(Q)$.

VI. INELASTIC-NEUTRON-SCATTERING SPECTRUM

The vibrational density of states is not directly accessible in experiments. The experimental technique that most closely reproduces the vibrational density of states is inelastic neutron scattering. Since Si and O have negligible incoherent-scattering cross sections, the one-phonon neutron-scattering function is given by[57,64]

$$S(\mathbf{Q},E) = \frac{1}{N\langle b^2\rangle} \sum_{II'} b_I b_{I'} e^{-(W_I + W_{I'})} e^{i\mathbf{Q}\cdot(\mathbf{R}_{I'} - \mathbf{R}_I)} \times \sum_n \hbar \frac{(\mathbf{Q}\cdot\boldsymbol{\xi}_I^n)(\mathbf{Q}\cdot\boldsymbol{\xi}_{I'}^n)}{2(M_I M_{I'})^{1/2}\omega_n} [n_B(\hbar\omega_n) + 1] \delta(E - \hbar\omega_n), \quad (21)$$

where the W_I are the exponents of the Debye-Waller factors, which for an isotropic amorphous system are given by

$$W_I(Q) = Q^2 \langle \mathbf{u}_I^2 \rangle / 6. \quad (22)$$

Through the neutron-scattering function, a generalized density of states can be defined as

$$G(Q,E) = e^{2\bar{W}} \frac{2\bar{m}E}{\hbar^2 Q^2} \frac{1}{n_B(E) + 1} S(Q,E), \quad (23)$$

where $\bar{m}^{-1} = \Sigma_I M_I^{-1}/N$ and $\bar{W} = Q^2\langle \mathbf{u}^2 \rangle / 6$. By averaging the generalized density of states $G(Q,E)$ over Q, we obtain an effective neutron density of states $G(E)$:

TABLE III. Average ($\langle Z^*_{iso}\rangle$) and standard deviations (ΔZ^*_{iso}) of the distribution of isotropic Born charges for the Si and O atoms in our models of v-SiO_2. The average percentual weights of isotropic ($\ell=0$) and anisotropic ($\ell=1$ and $\ell=2$) components are also given. The results of model III are taken from Ref. 15.

	Model I		Model II		Model III	
	Si	O	Si	O	Si	O
$\langle Z^*_{iso}\rangle$	3.298	−1.649	3.392	−1.696	3.177	−1.588
ΔZ^*_{iso}	0.106	0.062	0.079	0.046	0.121	0.078
$\ell=0$	97.94	80.03	97.77	78.42	96.94	82.27
$\ell=1$	0.33	0.13	0.24	0.11	0.46	0.16
$\ell=2$	1.73	19.84	1.99	21.48	2.60	17.56

$$G(E)=\frac{\int_{Q_1}^{Q_2} G(Q,E)dQ}{Q_2-Q_1}, \tag{24}$$

where Q_1 and Q_2 correspond to the limits of the experimentally investigated Q range.

In Fig. 4(b), the calculated effective neutron density of states of model I is compared to two sets of experimental data[49,50] and to the actual vibrational density of states. The agreement with experiment is overall very good. In particular, we note that our theoretical results reproduce well the density of states at low energy measured in Ref. 50. For the peak at ~100 meV, we record an excellent accord between theory and experiment,[49,50] lending support to the average Si-O-Si bond angle of model I (148°). The comparison between the effective neutron density of states and the actual one shows that for v-SiO_2 the relative intensities only undergo minor variations, in accord with previous studies.[28]

VII. INFRARED SPECTRA

A. Born charge tensors

The coupling between the atomic displacements and the electric field is described by the Born effective charge tensors $\boldsymbol{Z}^*$.[65] As described in Sec. IV, we calculated the charge tensors $\boldsymbol{Z}^*$ for all Si and O atoms in our models using a finite-difference scheme.

For analyzing the Born charge tensors, we adopted a decomposition in terms of the representations of the spatial rotations.[15] The decomposition consists of three terms labeled $\ell=0,1,2$. The $\ell=0$ term corresponds to the isotropic part,

$$\boldsymbol{Z}^*_{\ell=0}=Z^*_{iso}\delta_{ij}, \tag{25}$$

where $Z^*_{iso}=\mathrm{Tr}(\boldsymbol{Z}^*)/3$. The terms $\ell=1$ and $\ell=2$ constitute the anisotropic part and are expressed as

$$\boldsymbol{Z}^*_{\ell=1}=\frac{1}{2}(\boldsymbol{Z}^*-\boldsymbol{Z}^{*T}), \tag{26}$$

$$\boldsymbol{Z}^*_{\ell=2}=\frac{1}{2}(\boldsymbol{Z}^*+\boldsymbol{Z}^{*T})-\boldsymbol{Z}^*_{\ell=0}, \tag{27}$$

where $\boldsymbol{Z}^{*T}$ is the transpose of the $\boldsymbol{Z}^*$ tensor. Three parameters are required to describe the antisymmetric term $\ell=1$, while the traceless symmetric term $\ell=2$ is determined by five parameters. To quantify the respective weights of each component, we adopted the standard matricial norm.[15]

This analysis was carried out for the three models and the respective results are given in Table III. For Si atoms, the isotropic component ($\ell=0$) accounts for about 97% of the Born charge tensor, as a consequence of the local tetrahedral symmetry. Also for O atoms, the isotropic component is dominant, but the $\ell=2$ components give rise to a sizable contribution of ~20%. The contribution of the antisymmetric components $\ell=1$ is always found to be negligible.

The average isotropic charges in the three models show differences of at most 0.2 (Table III), which should be assigned to their different bond-angle and bond-length distributions. For the Si atoms of model I, we calculated an average isotropic charge of 3.3 with a standard deviation of 0.1. The average isotropic Born charge of the O atoms is −1.65 with a standard deviation of 0.05. For giving a more detailed description of the Born charge tensors of the O atoms, we adopted a local reference set based on the orientation of the Si-O-Si bond. We took the x direction along the bisector of Si-O-Si angle, the y direction normal to the plane of the Si-O-Si bridge, and the z direction orthogonal to the previous two. In this reference system, our calculation for model I gave the following average $\boldsymbol{Z}^*$ for O atoms:

$$\boldsymbol{Z}^*(\mathrm{O})=\begin{pmatrix} -1.10 & -0.01 & 0.00 \\ -0.01 & -1.04 & 0.00 \\ 0.00 & 0.00 & -2.80 \end{pmatrix}. \tag{28}$$

This average tensor is almost diagonal, with diagonal values typical for O bridge structures.[15,66] In particular, for the displacements along the stretching direction (z direction) the coupling is noticeably stronger than for the other directions.

B. Dielectric constant and dielectric function

The high-frequency dielectric tensor $\boldsymbol{\epsilon}_\infty$ is related to the dielectric susceptibility $\boldsymbol{\chi}$ through the usual relations of classical electrostatics:

TABLE IV. High-frequency (ϵ_∞) and static dielectric constants (ϵ_0) for models I–III of v-SiO_2. For models II and III, the reported values are taken from Refs. 13 and 16. Experimental values are taken from Refs. 67 and 68.

	ϵ_∞	ϵ_0
Model I	2.1	3.8
Model II	2.0	3.8
Model III	2.0	3.6
Expt.	2.1	3.8

$$(\epsilon_\infty)_{ij} = \delta_{ij} + 4\pi\chi_{ij}, \tag{29}$$

$$\chi_{ij} = -\frac{1}{V}\frac{\partial^2 E_{\mathrm{tot}}}{\partial \mathcal{E}_i \partial \mathcal{E}_j} = \frac{\partial P_i^{\mathrm{el}}}{\partial \mathcal{E}_j}, \tag{30}$$

where the derivatives with respect to the electric field should be evaluated at vanishing electric field. In this work, we calculated the derivative of the induced polarization with respect to electric field by finite differences, relying on the possibility of applying a finite electric field.[13,16] For all our models of v-SiO_2, the calculated high-frequency dielectric tensors are almost isotropic, as expected for an amorphous system.[19,20,46,47] We give in Table IV the isotropic average of these tensors: $\epsilon_\infty = \mathrm{Tr}(\boldsymbol{\epsilon}_\infty)/3$. All models give values which lie close to the experimental value. In particular, for model I, we obtained an average dielectric constant of 2.1, in agreement with the experimental value [2.1 (Ref. 67)]. The level of agreement is better than could be expected and likely results from the compensation of errors. Indeed, accurate calculations of the dielectric constant of α-quartz in the local-density approximation overestimate the experimental value by about 7%,[66] while the use of finite electric fields with finite cell sizes yields errors that underestimate the converged value.[31]

In the following, we describe the coupling to individual vibrational modes. It is therefore convenient to introduce the oscillator strengths $\boldsymbol{\mathcal{F}}^n$:

$$\mathcal{F}_j^n = \sum_{Ik} Z^*_{I,jk} \frac{\xi^n_{Ik}}{\sqrt{M_I}}. \tag{31}$$

We evaluated the static dielectric constant using the calculated vibrational frequencies and oscillator strengths:[15]

$$\epsilon_0 = \epsilon_\infty + \frac{4\pi}{3V}\sum_n \frac{|\boldsymbol{\mathcal{F}}^n|^2}{\omega_n^2}, \tag{32}$$

where V is the volume of the periodic simulation cell. For model I, we obtained $\epsilon_0 = 3.8$, in excellent agreement with the experimental value $\epsilon_0^{\mathrm{expt}} = 3.8$.[68] The values for the other models do not differ significantly and are summarized in Table IV.

The real and imaginary parts of the dielectric response function, $\epsilon_1(\omega)$ and $\epsilon_2(\omega)$, are given by[15,69]

$$\epsilon_1(\omega) = \epsilon_\infty - \frac{4\pi}{3V}\sum_n \frac{|\boldsymbol{\mathcal{F}}^n|^2}{\omega^2 - \omega_n^2}, \tag{33}$$

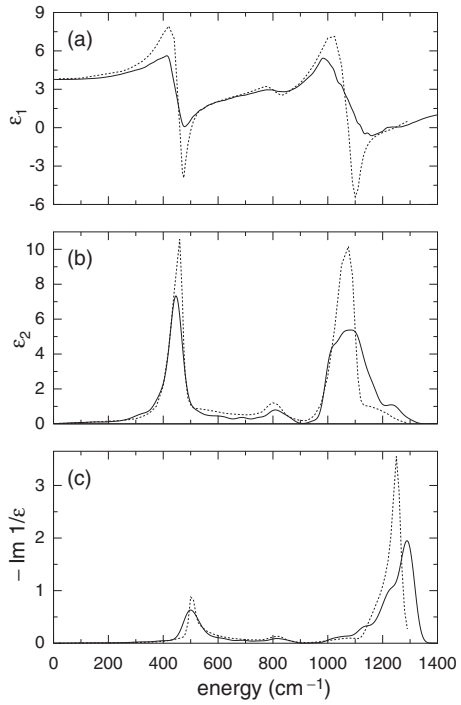

FIG. 10. (a) Real (ϵ_1) and (b) imaginary (ϵ_2) parts of the dielectric function, and (c) energy-loss function for model I of v-SiO_2 (solid curve) compared to experimental data of Ref. 67 (dotted curve). Lorentzian and Gaussian broadenings of 19 cm^{-1} were used for the real and imaginary parts, respectively.

$$\epsilon_2(\omega) = \frac{4\pi^2}{3V}\sum_n \frac{|\boldsymbol{\mathcal{F}}^n|^2}{2\omega_n}\delta(\omega - \omega_n). \tag{34}$$

The dielectric function described above gives access to all the dielectric properties. In particular, these include the energy-loss function which is obtained as $-\mathrm{Im}[1/\epsilon(\omega)]$. However, it was found convenient to access the latter function by a direct calculation:[16,69]

$$-\mathrm{Im}\left[\frac{1}{\epsilon(\omega)}\right] = \frac{4\pi^2}{V(\epsilon_\infty)^2}\sum_n \frac{(\mathbf{q}\cdot\boldsymbol{\mathcal{F}}^n)^2}{2\omega_n}\delta(\omega - \omega_n). \tag{35}$$

For isotropic systems, the energy-loss function in Eq. (35) can be averaged over all directions of $\mathbf{q}$. Here, we used the three Cartesian directions for this average.

In Figs. 10(a) and 10(b), we show the real and imaginary parts of the dielectric function calculated for model I together with the experimental result.[67] The agreement with experiment is of the same quality as for models II and III.[15,16] The calculation gives three principal resonances which occur in close correspondence of the experimental features. The real part shows typical S-shaped resonances in correspondence of the TO peaks in the imaginary part. Figure 10(c) shows the energy-loss function, which defines the positions of the LO peaks. Apart from the highest-frequency LO peak at $\sim$1250 cm^{-1}, the agreement with experiment is overall similar to that achieved for the dielectric function. We note that the comparison with experiment does not in-

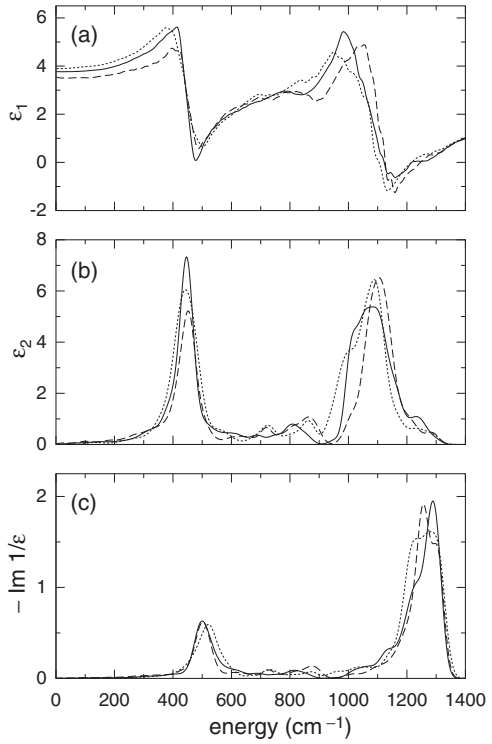

FIG. 11. (a) Real and (b) imaginary parts of the dielectric function and (c) energy-loss function for our models of v-SiO_2: model I (solid curve), model II (dotted curve), and model III (dashed curve). The results for model II were taken from Ref. 16. The imaginary part of model III was taken from Ref. 15. Lorentzian and Gaussian broadenings of 19 cm^{-1} were used.

clude the widths of the resonances, which are not modeled in our simulation approach.

In Fig. 11, we show the comparison between the dielectric and energy-loss functions of models I–III. The three models give spectra of overall similar shape. This similarity stems from the common short-range order which dominates the infrared spectra.[11,19] However, in the central band ranging between 300 and 700 cm^{-1}, and also in the high-frequency band ranging between 1000 and 1200 cm^{-1}, we observe minor differences between the calculated spectra. Since these bands arise from O bending and O stretching modes, respectively, these differences reflect differences in the Si-O-Si bond-angle and Si-O bond-length distributions. The function ϵ_2 of model I appears to give better global agreement with experiment than those of models II and III, particularly in the central part of the spectrum. Indeed, the spectra of the latter two models feature spurious peaks in the range of 700–900 cm^{-1} that are absent in the experimental spectrum (Fig. 10). However, the high-frequency peak at ~1100 is wider in models I and II than in model III. This feature should be attributed to the better relaxation of the atomic configuration in model III. Similar comments apply for the comparison between the calculated energy-loss spectra in Fig. 11(c).

In Table V, the frequencies of the main TO and LO features are summarized. The frequencies associated to the first and third resonances are overall well described with errors of at most ~30 cm^{-1}. The second resonance is very well described in model I, but models II and III overestimate the experimental frequency by ~50 cm^{-1}. This result further favors the Si-O-Si bond-angle distribution of model I. As far as the LO-TO splittings are concerned, all models give a good qualitative description, showing the largest splitting for the third resonance and the smallest splitting for the second one.

TABLE V. Frequencies (given in cm^{-1}) of the three main peaks of the imaginary part of the dielectric function (TO) and of the energy-loss function (LO). Δ indicates the splitting between corresponding LO and TO peaks. Experimental data are taken from Ref. 70.

	Model I	Model II	Model III	Expt.
TO_1	446	442	453	457
LO_1	500	522	501	507
Δ_1	54	80	48	50
TO_2	808	862	861	810
LO_2	816	872	873	820
Δ_2	8	10	12	10
TO_3	1084	1088	1106	1076
LO_3	1288	1282	1253	1256
Δ_3	204	194	147	180

C. Parametric model for infrared coupling

To assess the role of the local structural environment, we investigated correlations between the components of the Born charge tensors of the O atoms and the Si-O-Si bond angle. Figure 12(a) illustrates the correlation between the isotropic O Born charge and the corresponding Si-O-Si angle. The isotropic Born charge is found to decrease with

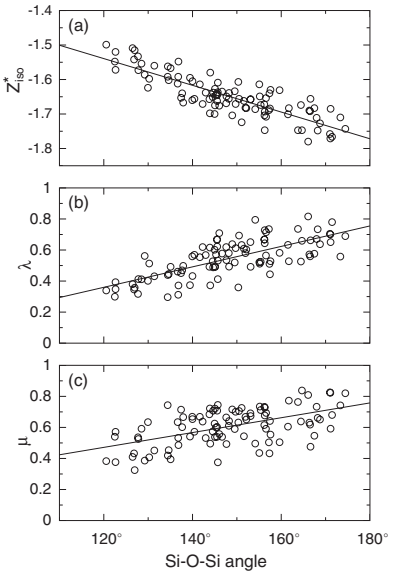

FIG. 12. Components of the oxygen Born charge tensors vs Si-O-Si angle for model I of v-SiO_2: (a) isotropic component $\langle Z^*_{iso} \rangle$ ($\ell=0$ term), (b) λ, and (c) μ components of the $\ell=2$ term (see text). The solid lines correspond to linear regressions.

increasing bond angle.[15] The trend is the same for all the three models with similar spreadings of data (not shown). Hence, the correlation in Fig. 12(a) holds irrespective of the Si-O-Si bond-angle distribution or ring statistics of the model. Other relevant components of the O Born charge tensors correspond to the diagonal of the traceless $\mathbf{Z}^*_{\ell=2}$ tensor defined in the local reference system described above. For each O atom, we defined the diagonal components λ and μ according to

$$\mathbf{Z}^*_{\ell=2} = \begin{pmatrix} \lambda & 0 & 0 \\ 0 & \mu & 0 \\ 0 & 0 & -\mu-\lambda \end{pmatrix}. \tag{36}$$

Figures 12(b) and 12(c) show that λ and μ also show a linear dependence on the Si-O-Si bond angle. These correlations offer the possibility of defining a simple parametrization of oxygen Born charge tensors in terms of only three functions which linearly depend on the Si-O-Si bond angle θ. For θ expressed in degrees, linear regressions of the data in Fig. 12 give

$$Z^*_{\rm iso}({\rm O}) = -1.65 - 0.0039(\theta - 148.2^\circ), \tag{37}$$

$$\lambda = 0.55 + 0.0066(\theta - 148.2^\circ), \tag{38}$$

$$\mu = 0.61 + 0.0048(\theta - 148.2^\circ). \tag{39}$$

It was pointed out in Ref. 15 that the isotropic Born charges satisfy a *local* dynamical charge neutrality rule. We found that this rule also holds for all the models of the present study (not shown), thereby supporting its generality. This rule establishes a relationship between the isotropic Born charges of the Si and O atoms belonging to the same tetrahedral unit:

$$Z^*_{\rm iso}({\rm Si}) \cong -\frac{1}{2}\sum_{\rm nn\ O} Z^*_{\rm iso}({\rm O}), \tag{40}$$

where the sum is restricted to the four nearest-neighbor O atoms of the Si atom. The occurrence of such a dynamical charge neutrality condition has been exploited to shed light onto the dielectric and infrared response of disordered oxide systems at low frequencies.[71,72]

In Fig. 13, we illustrate the effect of the Born charge tensors on the imaginary part of the dielectric function. Focusing on model I, we compare the result corresponding to using the full charge tensors with two parametric models for the Born charge tensors. The parametric models are designed to allow the modeling of infrared spectra without the necessity of obtaining the Born charge tensors through explicit calculations. The first parametric model is extremely simplified and consists of using isotropic Born charges for both Si and O atoms, fixed at their respective average values found for model I: $\langle Z^*_{\rm iso}({\rm Si})\rangle = 3.30$ and $\langle Z^*_{\rm iso}({\rm O})\rangle = -1.65$ (Table III). Figure 13 shows that such a parametric model does not properly describe the relative intensity between the first and the third resonances.[15] To improve upon this description, we considered a parametric model that also accounts for the $\ell = 2$ contribution to the Born charge tensors of the O atoms. For the O charge tensors, this parametric model accounts for

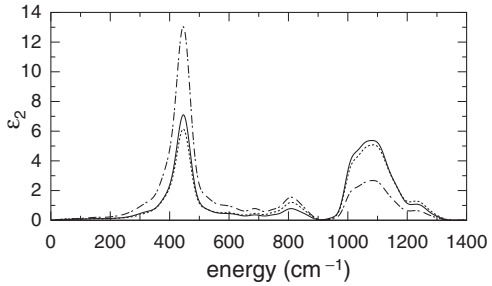

FIG. 13. Imaginary part of the dielectric function of model I of v-SiO_2 obtained using the full Born charge tensors (solid curve), compared to those obtained using solely the average values of the isotropic charges $Z^*_{\rm iso}$ of Si and O atoms (dot-dashed curve) and using the parametric model described in the text (dotted curve). A Gaussian broadening of 19 cm^{-1} was used.

the linear dependence of the tensor components $Z^*_{\rm iso}$, λ, and μ on the Si-O-Si angle through the relations given in Eqs. (37)–(39). For the Si charge tensors, we used isotropic tensors. For each atom, the value of the isotropic Born charge was determined on the basis of the isotropic charges of the neighboring O atoms through the local charge neutrality condition given in Eq. (40). The comparison in Fig. 13 shows that this parametric model yields a noticeable improvement upon the description achieved with solely isotropic charges, closely approaching the result obtained with Born charges calculated from first principles.

VIII. RAMAN SPECTRA

A. Raman cross section

In a first-order Stokes process of Raman scattering, an incoming photon of frequency Ω_L and polarization $\hat{\mathbf{e}}_L$ is scattered to an outgoing photon of frequency Ω_S and polarization $\hat{\mathbf{e}}_S$, creating a vibrational excitation of frequency $\omega_n = \Omega_L - \Omega_S$. In nonresonant conditions, i.e., when Ω_L is smaller than the band gap, the Placzek approximation[73] applies and the Raman cross section does not depend significantly on Ω_L (Ref. 74):

$$\frac{d^2\sigma}{d\Omega dE} \sim \sum_n |\hat{\mathbf{e}}_S \cdot \mathcal{R}^n \cdot \hat{\mathbf{e}}_L|^2 \frac{\hbar}{2\omega_n}[n_B(\hbar\omega_n)+1]\delta(E-\hbar\omega_n), \tag{41}$$

where E is the exchanged energy, $n(\hbar\omega_n)$ is the boson factor of Eq. (10), and the Ω_S^4 factor has been omitted because it varies negligibly in typical Raman scattering experiments on SiO_2. The second-rank tensors $\mathcal{R}^n$ are the Raman susceptibilities associated to the normal mode n:

$$\mathcal{R}^n_{ij} = \sqrt{V}\sum_{Ik} \frac{\partial \chi_{ij}}{\partial R_{Ik}} \frac{\xi^n_{Ik}}{\sqrt{M_I}}, \tag{42}$$

where the derivatives of the dielectric polarizability tensor χ_{ij} can be expressed as

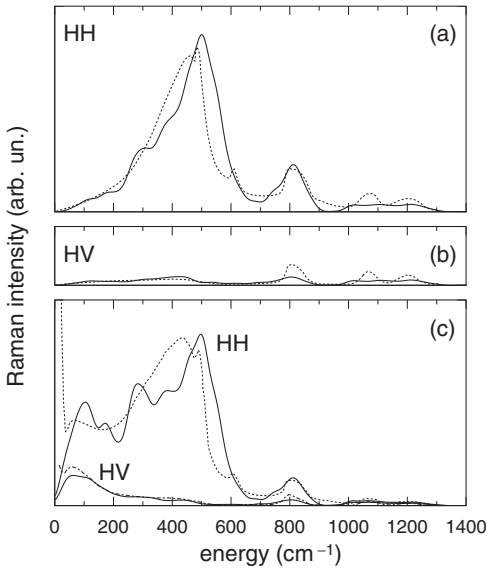

FIG. 14. Reduced (a) HH and (b) HV Raman spectra calculated for model I (solid curve), compared with the experimental data of Ref. 76 (dotted curve). (c) Nonreduced HH and HV Raman spectra of model I (solid curve) compared with the experimental data of Ref. 52 (dotted curve). The theoretical HH spectrum was scaled to match the integrated intensity of the experimental spectrum. The same scaling factor was then applied to the HV spectrum. A Gaussian broadening of 19 cm^{-1} was used.

$$\frac{\partial \chi_{ij}}{\partial R_{Ik}} = \frac{1}{V} \frac{\partial^2 F_{Ik}}{\partial \mathcal{E}_i \partial \mathcal{E}_j}. \tag{43}$$

In this equation the derivatives should be evaluated at vanishing electric field.

Raman spectra of disordered materials are usually recorded in configurations in which the polarizations of incoming and outgoing photons are either parallel (HH) or perpendicular (HV).[74] To omit the main thermal dependence, the experimental Raman cross section is often given in a reduced form:

$$\left.\frac{d^2\sigma}{d\Omega dE}\right|_{\text{red}} \sim \sum_n |\hat{\mathbf{e}}_S \cdot \mathcal{R}^n \cdot \hat{\mathbf{e}}_L|^2 \delta(E - \hbar\omega_n). \tag{44}$$

B. Raman spectra and medium-range order

In the present work, we focused on nonresonant Raman spectra. The derivatives in Eq. (43) were evaluated through the application of finite electric fields,[13] as detailed in Appendix A. We calculated HH and HV spectra by taking appropriate orientational averages.[74,75]

In Figs. 14(a) and 14(b), we report both the reduced and nonreduced HH and HV Raman spectra of model I of v-SiO_2 compared to experimental data taken from Refs. 52 and 76. The experimental Raman spectra are well consolidated and have been confirmed by a large body of experimental work.[77] Overall, we register good agreement with experiment. The small differences between experiment and theory appearing in the reduced spectra below ~400 cm^{-1} are amplified in the nonreduced spectra because of the boson factor [Eq. (10)]. The calculated HV spectrum in Fig. 14(c) features a clear peak in correspondence of the experimental boson peak at ~50 cm^{-1}. In models II and III this feature is unresolved and instead spurious features occur at ~150 cm^{-1} (not shown). Thus, model I gives the best description of the low-frequency region of the Raman spectra, presumably due its larger size (cf. Table I).

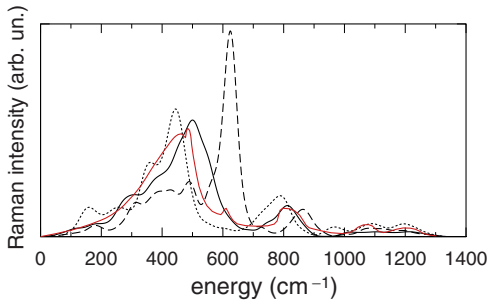

FIG. 15. (Color online) Calculated reduced HH Raman spectra of model I (solid curve), model II (dotted curve), and model III (dashed curve), compared with the experimental data of Ref. 76 (gray/red). The result for model II is taken from Ref. 16. A Gaussian broadening of 19 cm^{-1} is used.

While the HV spectrum is reminiscent of the vibrational density of states,[75] the HH Raman spectrum is dominated by the coupling factor associated to oxygen bending motions.[11] Through this property, the HH Raman spectrum is particularly sensitive to relative arrangement of tetrahedra in the SiO_2 network. In Fig. 15, the reduced HH Raman spectra of our three models of v-SiO_2 are compared. The three spectra show significant differences, especially in the range of 300–700 cm^{-1}, i.e., for the bending band. The calculated Raman spectra reflect the differences in the corresponding Si-O-Si distributions (Fig. 1) and ring statistics (Fig. 2). We remark that as the average Si-O-Si bond angle in the model decreases, the Raman intensity in the range of 300–700 cm^{-1} shifts toward higher frequencies.

The role of small ring structures deserves particular attention. The experimental HH Raman spectrum of v-SiO_2 shows two particularly sharp lines at 495 and 606 cm^{-1}, known as D_1 and D_2.[76,78] A first-principles investigation unambiguously assigned the origin of these lines to breathing vibrations of oxygen atoms in four-membered and three-membered rings, respectively.[12] From the intensities of these lines, an estimate of the concentration of three-membered and four-membered rings in v-SiO_2 could be derived.[11] A similar analysis applied to v-B_2O_3 succeeded in giving an estimate of the fraction of B atoms in boroxol rings.[20]

The large peak occurring at ~620 cm^{-1} in the Raman spectrum of model III (Fig. 15) corresponds to vibrations in three-membered rings, and its intensity reflects the high concentration of such rings in this model (cf. Fig. 2).[11] Model II is devoid of three-membered rings and consequently its Raman spectrum shows a low intensity in the range around 600 cm^{-1}.[16] Model I only contains a single three-membered ring, and its intensity does not stand out in the calculated spectrum since all modes are artificially broadened in the same way in Fig. 15. Nevertheless, the projection on the

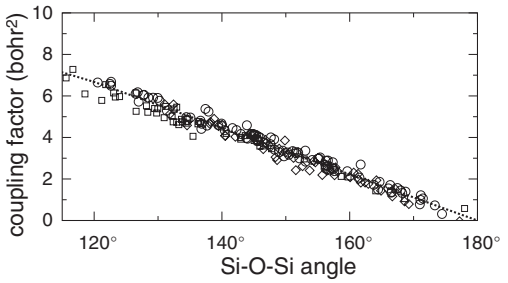

FIG. 16. Raman coupling factors f_I vs Si-O-Si angle, calculated for O atoms in model I (circles), model II (diamonds), and model III (squares). The dashed curve corresponds to the fit of the coupling factors of model I according to Eq. (46).

vibrational ring mode prior to the calculation of the Raman cross section gives a peak at ~610 cm^{-1}, in close correspondence with the experimental Raman line D_2 at 606 cm^{-1}.

As shown in Table II, all models feature concentrations of four-membered rings in excess of the estimate derived from the intensity of the D_1 line.[11] The best description of this feature is provided by model II. Its Raman spectrum features a main peak which is shifted toward lower frequencies than in the other two models, in closer agreement with the experimental spectrum. While model I gives an overall accurate description of the vibrational properties, it fails to give an accurate description of the main Raman peak. Indeed, model I shows a high concentration of four-membered rings comprising ~42% of the O atoms, thereby considerably overestimating the value of 0.36% derived from the intensity of the D_1 line (Table II).[11] Consequently, the Raman spectrum of model I mainly arises from oxygen bending motions in four-membered rings, resulting in a principal Raman peak at ~500 cm^{-1}, significantly shifted toward higher frequencies with respect to its experimental counterpart (~450 cm^{-1}). Indeed, the projection on oxygen bending motions in four-membered rings prior to the calculation of the Raman cross section results in a very intense peak at ~510 cm^{-1}, in good agreement with the experimental position of the D_1 line (~495 cm^{-1}).

C. Parametric model for Raman coupling

Since the relevant coupling tensor $\partial\boldsymbol{\chi}/\partial\mathbf{R}$ associated to the dominant oxygen bending motions is almost isotropic, a scalar coupling factor can be calculated for each O atom:

$$f_I = \frac{1}{3} V \,\mathrm{Tr}\left(\sum_k \frac{\partial \boldsymbol{\chi}}{\partial R_{Ik}} e^b_{Ik} \right), \tag{45}$$

where $\mathbf{e}^b$ corresponds to the bisector direction of the Si-O-Si unit to which the O atom belongs.[11] The coupling factors f_I defined in this way are independent of volume. Figure 16 shows the correlation between the calculated coupling factors f_I and the Si-O-Si bond angle θ_I for our three models. All models consistently give the same dependence.

The observed dependence can be expressed by the relation[11]

TABLE VI. Bond-polarizability-model parameters (expressed in $bohr^2$) as derived from models I–III and from all models taken together. The second column specifies the way the electric field was applied in the calculation of the coupling tensors, i.e., either through a finite field (FF) or according to perturbation theory (PT). The PT parameters for model III and for α-quartz are taken from Refs. 11 and 79, respectively.

		α	β	γ
All models	FF	39.3	8.8	2.2
Model I	FF	40.8	9.3	2.4
Model II	FF	41.2	8.9	2.1
Model III	FF	38.5	8.4	2.3
Model III	PT	46.5	10.3	2.2
α-quartz	PT	45.5	11.6	3.3

$$f_I = (\alpha/3)\cos(\theta_I/2), \tag{46}$$

which holds for a system of regular tetrahedral units described within the bond-polarizability model.[11] The parameter α is one of the three parameters of this model (see Appendix B). For each model, we derived an optimal value of α through a one-parameter least-squares fit of the coupling factors in Fig. 16. The obtained values differ by at most a few percent from the value of α obtained through a global optimization of the data of all models. The obtained values of α are summarized in Table VI.

The good description provided by the relationship in Eq. (46) lends support to the use of the bond-polarizability model[80] as a viable parametric model for the Raman couplings. The use of the bond-polarizability model is further supported by previous successful applications to α-quartz,[79,81] vitreous SiO_2,[82,83] and compressed v-SiO_2.[83] We therefore completed the set of bond-polarizability parameters by determining the two other parameters, β and γ (cf. Appendix B), to be associated to the parameter α fixed above. We obtained optimal β and γ parameters by minimizing the sum of squared differences between the components of the tensor $\partial\boldsymbol{\chi}/\partial\boldsymbol{R}$ calculated within the bond-polarizability model and within our first-principles scheme. This procedure resulted in the parameters summarized in Table VI. In Fig. 17, we show the HH Raman spectrum of model I calculated through this set of bond-polarizability-model parameters. The comparison with the corresponding first-principles spectrum demonstrates the quality of our parametric model.

In a previous study, the coupling tensors $\partial\boldsymbol{\chi}/\partial\boldsymbol{R}$ were obtained by treating the electric field in a perturbative manner.[11,47] Application to model III led to an optimal value of α=46.5 $bohr^2$, slightly larger than the value obtained in the present work for the same model through the use of finite electric fields (cf. Table VI). The difference between the two calculations originates from the incomplete k-point (viz. Γ-point-only) sampling used in the two schemes and provides an estimate of the error of the calculations.[31] Since the coupling to bending modes dominates the HH Raman spectra, this difference mostly results in a change in normalization, affecting the comparison with experiment in a minor way.

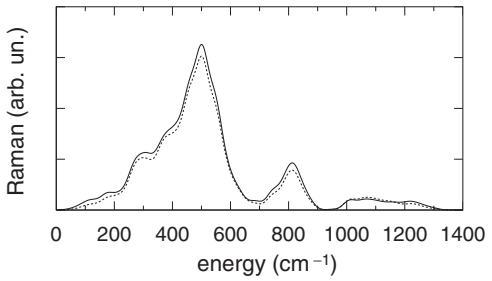

FIG. 17. Reduced HH Raman spectrum of model I calculated with globally optimized bond-polarizability parameters (dotted curve), compared to the corresponding spectrum calculated fully from first principles (solid curve). A Gaussian broadening of 19 cm^{-1} was used.

As a final remark concerning the derived parameters, it is worth emphasizing that these parameters mainly depend on the properties of the Si-O bond rather than on the type of disorder occurring in the network. In Table VI, we report the optimal bond-polarizability parameters derived for α-quartz through a perturbation approach.[79] Having expressed these parameters in the same units as the other parameters in Table VI, we can compare them with those for model III of v-SiO_2 derived through a similar perturbation approach.[11,47] This comparison clearly indicates that the derivatives of the polarizability of the Si-O bond in vitreous silica are very close to those of the Si-O bond in α-quartz.

IX. CONCLUSIONS

In this work, we addressed the vibrational spectra of vitreous silica through a comparative study involving three model structures. All the investigated models consist of corner-sharing tetrahedra with very similar short-range-order properties. However, the models differ considerably as far as their medium-range properties are concerned, such as the Si-O-Si bond-angle distribution and the ring statistics. In particular, we introduced in the present work a model structure (model I) which incorporates several structural features inferred from previous investigations, in the attempt of improving the comparison between experiment and theory.

The validation of structural models occurs through the consideration of the results of a large set of experimental techniques, including not only typical structural probes, such as neutron and x-ray diffractions, but also vibrational spectra as obtained through inelastic neutron scattering, infrared absorption, and Raman scattering. One specific goal of the present investigation is to determine to what extent specific experimental features are informative about the underlying medium-range structural properties of the silica network.

Our investigation started by considering the neutron and x-ray structure factors. Overall, the comparison between calculated and measured total structure factors is very good for all considered models, indicating that these structure factors are not sufficiently sensitive to the medium-range structure. Similar agreement also holds for the Si-O and O-O partial structure factors. However, the Si-Si partial structure factor is found to be very informative about the Si-O-Si bond-angle distribution, allowing for discrimination between models through comparison with experiment.

We then considered three kinds of vibrational spectra: the inelastic neutron spectrum, the infrared spectra, and the Raman spectra. For the inelastic neutron spectrum and the various infrared spectra, the agreement with experiment was found to be generally quite good, irrespective of the considered models. This indicates that these spectra only provide limited information on the medium-range structure. The only exception concerns the feature at $\sim$800 cm^{-1}, which shows a clear correlation with the average Si-O-Si bond angle, shifting to higher frequencies when the average angle decreases. At variance, the parallel-polarized Raman spectrum is shown to be highly sensitive to the medium-range organization of the network. This high sensitivity directly stems from the predominance of the Raman coupling to oxygen bending motions. Through this dependence, the distribution of the Raman intensity between 300 and 700 cm^{-1} appears to be very informative about the concentrations of three-membered and four-membered rings. Recent estimates derived from experimental Raman spectra give very small concentrations of both three-membered and four-membered rings. Typical model structures of 100–200 atoms overestimate at least one of these concentrations by 1–2 orders of magnitude. The adverse effect on the Raman spectrum is particularly severe when the concentration of three-membered rings is overestimated because the corresponding feature falls above the principal Raman peak and is clearly distinguishable. The effect is less apparent for four-membered rings which yield a peak lying in the range of the principal Raman peak.

The Si-Si partial structure factor, the position of the peak at $\sim$800 cm^{-1} in the three vibrational spectra considered in this work, and the strong dependence of the Raman spectrum on the concentrations of small rings are features that can be used for refining structural models of v-SiO_2. Among the three models in this work, model I reproduces in the best way the experimental Si-Si partial structure factor and the position of the peak at $\sim$800 cm^{-1} in the measured vibrational spectra, thereby lending support to its Si-O-Si bond-angle distribution. This distribution is characterized by an average angle of 148° and a standard deviation of 13°. The Raman spectra calculated for the three models show dramatic differences which can be assigned to their different ring statistics. The observed differences between the calculated and the measured Raman spectra are consistent with the concentrations of small rings in the models. The principal Raman peak at 450 cm^{-1} is best reproduced by model II, which also best describes the concentrations of small rings. Model I also gives a fair description of the main Raman peak, but its intensity is found to be slightly shifted to higher frequencies because of an excess of four-membered rings. Hence, this study indicates that the considered experimental data are globally consistent with a medium-range structure characterized by an average Si-O-Si bond angle of 148° and with small-ring concentrations as derived from the intensity of the experimental Raman defect lines. Our work provides an illustration of how structural models of v-SiO_2 can successively be improved by establishing a virtuous cycle that involves comparison between theory and experiment. A similar ap-

proach has recently also been applied to the modeling of vitreous GeO_2 and vitreous $GeSe_2$.[19,21]

The present study also provides parametric models to describe the infrared and Raman couplings. For the infrared coupling, we first focused on the Born charge tensors of the oxygen atoms, finding a parametrization of both the isotropic and the traceless anisotropic components in terms of the Si-O-Si bond angle. The Born charge of the silicon atoms was then determined through the application of the local dynamical charge neutrality condition. For the Raman coupling, we opted for a description in terms of the bond-polarizability model. We demonstrated the reliability of both parametric models in reproducing the vibrational spectra by comparison with spectra calculated from first principles.

ACKNOWLEDGMENTS

The authors thank C. J. Benmore for providing them with the experimental data of Ref. 7 prior to publication. Support from the Swiss National Science Foundation is acknowledged (Grant No. 200021-103562/1). The calculations were performed on the cluster PLEIADES of EPFL and on the computational facilities of DIT-EPFL, CSEA-EPFL, and the Swiss Center for Scientific Computing.

APPENDIX A: CALCULATION OF RAMAN COUPLING TENSORS BY FINITE DIFFERENCES

We calculated the tensors $\partial\chi_{ij}/\partial R_{Ik}$ of model I as second derivatives of the atomic forces with respect to the electric field, according to Eq. (43). We obtained these second derivatives numerically through the application of finite electric fields.[13]

For the diagonal terms $\partial\chi_{ii}/\partial R_{Ik}$, we used the following formula:

$$\left.\frac{\partial^2 F}{\partial^2 \mathcal{E}}\right|_0 \simeq \frac{1}{12h^2}[-F(-2h)+16F(-h)-30F(0)+16F(h) - F(2h)], \quad \text{(A1)}$$

where $F(\mathcal{E})$ indicates the desired atomic force component as a function of the finite field $\mathcal{E}$ taken along a Cartesian direction. We took electric fields defined by $h=0.0025$ a.u.

For the off-diagonal ($i \neq j$) terms of $\partial\chi_{ij}/\partial R_{Ik}$, we used the following finite-difference scheme, which can be derived from the Taylor development of atomic force component $F(\mathcal{E}_i,\mathcal{E}_j)$ in terms of the electric fields $\mathcal{E}_i$ and $\mathcal{E}_j$ (Ref. 84):

$$\left.\frac{\partial^2 F}{\partial \mathcal{E}_i\, \partial \mathcal{E}_j}\right|_0 \simeq \frac{1}{4\tilde{h}^2}[F(\tilde{h},\tilde{h})+F(-\tilde{h},-\tilde{h})-F(-\tilde{h},\tilde{h}) - F(\tilde{h},-\tilde{h})], \quad \text{(A2)}$$

where we took $\tilde{h}=h/\sqrt{2}$ to preserve the same stride as for the diagonal terms. The calculation of the mixed term relies on the possibility of applying simultaneously finite fields along two different Cartesian directions. This feature has been implemented in the CP code of the QUANTUM-ESPRESSO package.[27] Figure 18 shows the number of finite electric field calculations that are required for evaluating the tensors $\partial\chi_{ij}/\partial R_{Ik}$ pertaining to a couple of Cartesian directions. The full tensors are obtained through 25 self-consistent minimizations. No sensible variation in the calculated spectra was found when the second-order derivatives in Eq. (43) were estimated with a three-point formula.

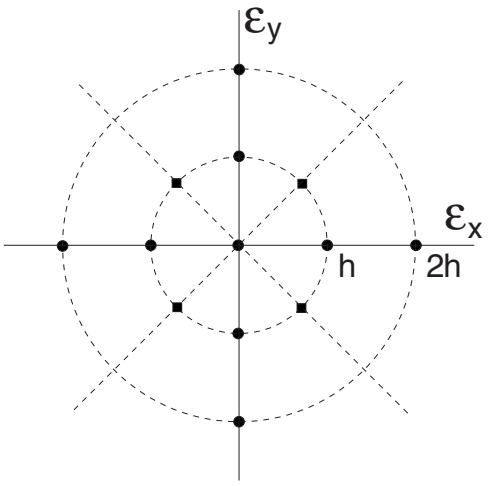

FIG. 18. Schematic illustration of the number of independent finite electric field calculations that are required for evaluating the diagonal (disks) and off-diagonal (filled squares) components of the tensors $\partial\chi_{ij}/\partial R_{Ik}$ pertaining to a couple of Cartesian directions.

APPENDIX B: PARAMETERS OF BOND-POLARIZABILITY MODEL

In the bond-polarizability model, the polarizability is described in terms of bond contributions:

$$\alpha_{ij} = \frac{1}{3}(2\alpha_p+\alpha_l)\delta_{ij} + (\alpha_l-\alpha_p)\left(\frac{R_i R_j}{R^2}-\frac{1}{3}\delta_{ij}\right), \quad \text{(B1)}$$

where $\mathbf{R}=\mathbf{R}_J-\mathbf{R}_I$ is a vector which defines the direction and the distance of a pair of nearest-neighbor atoms at sites $\mathbf{R}_I$ and $\mathbf{R}_J$. The parameters α_l and α_p correspond to the longitudinal and perpendicular bond polarizabilities, respectively. The bond-polarizability model further assumes that the bond polarizabilities α_l and α_p only depend on the length of the bond. Thus, the derivative of the bond polarizability with respect to the displacement of atom J reads

$$\frac{\partial\alpha_{ij}}{\partial R_{Jk}} = \frac{1}{3}(2\alpha_p'+\alpha_l')\delta_{ij}\hat{R}_k + (\alpha_l'-\alpha_p')\left(\hat{R}_i\hat{R}_j-\frac{1}{3}\delta_{ij}\right)\hat{R}_k + \frac{(\alpha_l-\alpha_p)}{R}(\delta_{ik}\hat{R}_j+\delta_{jk}\hat{R}_i-2\hat{R}_i\hat{R}_j\hat{R}_k), \quad \text{(B2)}$$

where $\hat{\mathbf{R}}$ is a unit vector along $\mathbf{R}$, and α_l' and α_p' are the derivatives of the bond polarizabilities with respect to the bond length. Therefore, when only one type of bond occurs, the bond-polarizability model is completely defined by three parameters:

$$\alpha = 2\alpha_p' + \alpha_l', \quad \beta = \alpha_l' - \alpha_p', \quad \gamma = (\alpha_l - \alpha_p)/R. \quad \text{(B3)}$$

In this approximation, the tensors $\partial\boldsymbol{\chi}/\partial\boldsymbol{R}$ appearing in Eq. (43) are obtained by dividing the tensor $\partial\boldsymbol{\alpha}/\partial\boldsymbol{R}$ by the volume V.

[1] *Optical Fiber Communications*, edited by Li Tingye (Academic, Orlando, 1985), Vol. 1, p. 9; B. J. Ainslie and C. R. Day, J. Lightwave Technol. **4**, 967 (1986).
[2] M. L. Green, E. P. Gusev, R. Degraeve, and E. L. Garfunkel, J. Appl. Phys. **90**, 2057 (2001).
[3] W. H. Zachariasen, J. Am. Chem. Soc. **54**, 3841 (1932); B. E. Warren, Phys. Rev. **45**, 657 (1934).
[4] D. I. Grimley, A. C. Wright, and R. N. Sinclair, J. Non-Cryst. Solids **119**, 49 (1990).
[5] R. L. Mozzi and B. E. Warren, J. Appl. Crystallogr. **2**, 164 (1969).
[6] J. Neuefeind and K. D. Liss, Ber. Bunsenges. Phys. Chem **100**, 1341 (1996).
[7] Q. Mei, C. J. Benmore, S. Sen, R. Sharma, and J. L. Yarger, Phys. Rev. B **78**, 144204 (2008).
[8] F. Mauri, A. Pasquarello, B. G. Pfrommer, Y. G. Yoon, and S. G. Louie, Phys. Rev. B **62**, R4786 (2000).
[9] T. M. Clark, P. J. Grandinetti, P. Florian, and J. F. Stebbins, Phys. Rev. B **70**, 064202 (2004).
[10] S. V. King, Nature (London) **213**, 1112 (1967).
[11] P. Umari, X. Gonze, and A. Pasquarello, Phys. Rev. Lett. **90**, 027401 (2003).
[12] A. Pasquarello and R. Car, Phys. Rev. Lett. **80**, 5145 (1998).
[13] P. Umari and A. Pasquarello, Phys. Rev. Lett. **89**, 157602 (2002).
[14] J. Sarnthein, A. Pasquarello, and R. Car, Science **275**, 1925 (1997).
[15] A. Pasquarello and R. Car, Phys. Rev. Lett. **79**, 1766 (1997).
[16] P. Umari and A. Pasquarello, Diamond Relat. Mater. **14**, 1255 (2005).
[17] P. Umari and A. Pasquarello, Phys. Rev. Lett. **98**, 176402 (2007).
[18] L. Giacomazzi, P. Umari, and A. Pasquarello, Phys. Rev. Lett. **95**, 075505 (2005).
[19] L. Giacomazzi, P. Umari, and A. Pasquarello, Phys. Rev. B **74**, 155208 (2006).
[20] P. Umari and A. Pasquarello, Phys. Rev. Lett. **95**, 137401 (2005).
[21] L. Giacomazzi, C. Massobrio, and A. Pasquarello, Phys. Rev. B **75**, 174207 (2007).
[22] L. Giacomazzi and A. Pasquarello, J. Phys.: Condens. Matter **19**, 415112 (2007).
[23] R. Car and M. Parrinello, Phys. Rev. Lett. **55**, 2471 (1985).
[24] A. Pasquarello, K. Laasonen, R. Car, C. Y. Lee, and D. Vanderbilt, Phys. Rev. Lett. **69**, 1982 (1992); K. Laasonen, A. Pasquarello, R. Car, C. Y. Lee, and D. Vanderbilt, Phys. Rev. B **47**, 10142 (1993).
[25] G. B. Bachelet, D. R. Hamann, and M. Schlüter, Phys. Rev. B **26**, 4199 (1982).
[26] D. Vanderbilt, Phys. Rev. B **41**, 7892 (1990).
[27] http://www.quantum-espresso.org
[28] A. Pasquarello, J. Sarnthein, and R. Car, Phys. Rev. B **57**, 14133 (1998).
[29] S. Baroni, S. de Gironcoli, A. Dal Corso, and P. Giannozzi, Rev. Mod. Phys. **73**, 515 (2001).
[30] X. Gonze and C. Lee, Phys. Rev. B **55**, 10355 (1997).
[31] P. Umari and A. Pasquarello, Phys. Rev. B **68**, 085114 (2003).
[32] R. M. Van Ginhoven, H. Jónsson, and L. R. Corrales, Phys. Rev. B **71**, 024208 (2005).
[33] A. Bongiorno and A. Pasquarello, Phys. Rev. Lett. **88**, 125901 (2002).
[34] M. Benoit, S. Ispas, P. Jund, and R. Jullien, Eur. Phys. J. B **13**, 631 (2000).
[35] B. W. H. van Beest, G. J. Kramer, and R. A. van Santen, Phys. Rev. Lett. **64**, 1955 (1990).
[36] K. Vollmayr, W. Kob, and K. Binder, Phys. Rev. B **54**, 15808 (1996).
[37] J. Sarnthein, A. Pasquarello, and R. Car, Phys. Rev. B **52**, 12690 (1995); Phys. Rev. Lett. **74**, 4682 (1995).
[38] X. L. Yuan and A. N. Cormack, Comput. Mater. Sci. **24**, 343 (2002).
[39] R. J. Bell and P. Dean, Philos. Mag. **25**, 1381 (1972).
[40] J. P. Rino, I. Ebbsjo, R. K. Kalia, A. Nakano, and P. Vashishta, Phys. Rev. B **47**, 3053 (1993).
[41] D. Stöffler and J. Arndt, Naturwiss. **56**, 100 (1969).
[42] N. Binggeli, N. Troullier, J. L. Martins, and J. R. Chelikowsky, Phys. Rev. B **44**, 4771 (1991); F. Giustino and A. Pasquarello, Phys. Rev. Lett. **96**, 216403 (2006).
[43] F. J. Himpsel, Surf. Sci. **168**, 764 (1986); F. J. Grunthaner and P. J. Grunthaner, Mater. Sci. Rep. **1**, 65 (1986).
[44] P. Broqvist, J. F. Binder, and A. Pasquarello (unpublished).
[45] M. Born and K. Huang, *Dynamical Theory of Crystal Lattices* (Oxford University Press, Oxford, 1954).
[46] D. Donadio, M. Bernasconi, and F. Tassone, Phys. Rev. B **68**, 134202 (2003).
[47] P. Umari, X. Gonze, and A. Pasquarello, Phys. Rev. B **69**, 235102 (2004).
[48] R. Resta, Rev. Mod. Phys. **66**, 899 (1994).
[49] J. M. Carpenter and D. L. Price, Phys. Rev. Lett. **54**, 441 (1985).
[50] U. Buchenau, M. Prager, N. Nücker, A. J. Dianoux, N. Ahmad, and W. A. Phillips, Phys. Rev. B **34**, 5665 (1986).
[51] P. N. Sen and M. F. Thorpe, Phys. Rev. B **15**, 4030 (1977).
[52] F. L. Galeener, Phys. Rev. B **19**, 4292 (1979); J. Non-Cryst. Solids **40**, 527 (1980).
[53] Y. Waseda, *The Structure of Non-crystalline Materials* (McGraw-Hill, New York, 1980).
[54] A. Pasquarello, Phys. Rev. B **61**, 3951 (2000).
[55] D. L. Price and A. Pasquarello, Phys. Rev. B **59**, 5 (1999).
[56] C. Massobrio, A. Pasquarello, and R. Car, Phys. Rev. B **64**, 144205 (2001).

[57] D. L. Price and J. M. Carpenter, J. Non-Cryst. Solids **92**, 153 (1987).
[58] S. Susman, K. J. Volin, D. L. Price, M. Grimsditch, J. P. Rino, R. K. Kalia, P. Vashishta, G. Gwanmesia, Y. Wang, and R. C. Liebermann, Phys. Rev. B **43**, 1194 (1991).
[59] Q. Mei, C. J. Benmore, and J. K. R. Weber, Phys. Rev. Lett. **98**, 057802 (2007).
[60] Table 6.1.1.4 of *International Tables for Crystallography*, edited by A. J. C. Wilson (Kluwer, Dordrecht, 1992), Vol. C, pp. 500–502.
[61] I. T. Penfold and P. S. Salmon, Phys. Rev. Lett. **67**, 97 (1991).
[62] C. Massobrio and A. Pasquarello, Phys. Rev. B **68**, 020201 (2003); C. Massobrio, M. Celino, and A. Pasquarello, *ibid.* **70**, 174202 (2004).
[63] A. B. Bhatia and D. E. Thornton, Phys. Rev. B **2**, 3004 (1970).
[64] D. L. Price and K. Sköld, in *Neutron Scattering*, edited by K. Sköld and D. L. Price (Academic, Orlando, 1986), p. 1.
[65] Ph. Ghosez, J. P. Michenaud, and X. Gonze, Phys. Rev. B **58**, 6224 (1998).
[66] X. Gonze, D. C. Allan, and M. P. Teter, Phys. Rev. Lett. **68**, 3603 (1992); *Phonon Scattering in Condensed Matter VII*, edited by M. Meissner and R. O. Pohl (Springer-Verlag, Berlin, 1993), p. 511.
[67] H. R. Philipp, in *Handbook of Optical Constants of Solids*, edited by D. Palik (Academic, San Diego, 1998), p. 749.
[68] *Handbook of Chemistry and Physics*, edited by D. R. Lide (CRC, New York, 1998).
[69] M. F. Thorpe and S. W. de Leeuw, Phys. Rev. B **33**, 8490 (1986).
[70] C. T. Kirk, Phys. Rev. B **38**, 1255 (1988).
[71] G.-M. Rignanese, F. Detraux, X. Gonze, A. Bongiorno, and A. Pasquarello, Phys. Rev. Lett. **89**, 117601 (2002).
[72] S. N. Taraskin, S. I. Simdyankin, S. R. Elliott, J. R. Neilson, and T. Lo, Phys. Rev. Lett. **97**, 055504 (2006).
[73] G. Placzek, in *Handbuck der Radiologie*, edited by E. Marx (Akademische Verlagsgesellshaft, Leipzig, 1934), Vol. 6, p. 209.
[74] *Light Scattering in Solids II*, edited by M. Cardona and G. Güntherod (Springer-Verlag, Berlin, 1982).
[75] P. Umari and A. Pasquarello, J. Phys.: Condens. Matter **15**, S1547 (2003).
[76] F. L. Galeener and G. Lucovsky, Phys. Rev. Lett. **37**, 1474 (1976); F. L. Galeener, Solid State Commun. **44**, 1037 (1982).
[77] P. Dumas, J. Corset, Y. Levy, and V. Neuman, J. Raman Spectrosc. **13**, 134 (1982); P. McMillan, B. Piriou, and R. Couty, J. Chem. Phys. **81**, 4234 (1984); R. J. Hemley, H. K. Mao, P. M. Bell, and B. O. Mysen, Phys. Rev. Lett. **57**, 747 (1986); B. Hehlen, E. Courtens, R. Vacher, A. Yamanaka, M. Kataoka, and K. Inoue, *ibid.* **84**, 5355 (2000); A. Fontana, F. Rossi, and E. Fabiani, J. Non-Cryst. Solids **352**, 4601 (2006).
[78] F. L. Galeener, R. A. Barrio, E. Martinez, and R. J. Elliott, Phys. Rev. Lett. **53**, 2429 (1984).
[79] P. Umari, A. Pasquarello, and A. Dal Corso, Phys. Rev. B **63**, 094305 (2001).
[80] M. V. Wolkenstein, C. R. Acad. Sci. URSS **30**, 791 (1941); M. A. Eliashevich and M. V. Wolkenstein, J. Phys. (USSR) **9**, 101 (1944).
[81] Y. Liang, C. R. Miranda, and S. Scandolo, J. Chem. Phys. **125**, 194524 (2006).
[82] P. Umari and A. Pasquarello, Physica B **316-317**, 572 (2002).
[83] A. Rahmani, M. Benoit, and C. Benoit, Phys. Rev. B **68**, 184202 (2003).
[84] L. Lapidus and G. F. Pinder, *Numerical Solutions of Partial Differential Equations in Science and Engineering* (Wiley-Interscience, New York, 1982), p. 35.